Dynamics of Coherent Structures in Turbulent Rayleigh-Bénard Convection by Lagrangian Particle Tracking of Long-Lived Helium Filled Soap Bubbles

J. Bosbach[1,*], D. Schanz[1], P. Godbersen[1], A. Schröder[1,2]
1: Department of Experimental Methods, Institute of Aerodynamics and Flow Technology,
German Aerospace Center (DLR), Göttingen, Germany
2: Brandenburgisch Technische Universität (BTU) Cottbus-Senftenberg, Germany
* Correspondent author: Johannes.Bosbach@dlr.de

Keywords: Shake-The-Box, Lagrangian Particle Tracking, data assimilation, helium-filled soap bubbles, Rayleigh-Bénard convection

ABSTRACT

We present spatially and temporally resolved velocity and acceleration measurements of turbulent Rayleigh-Bénard convection covering the complete volume of a cylindrical sample with aspect ratio one. Using the "Shake-The-Box" Lagrangian Particle Tracking algorithm, we were able to instantaneously track more than 560,000 particles in the complete sample volume (~ 1 m^3), corresponding to mean inter-particle distances of less than 8 volume-averaged Kolmogorov lengths. We used the data assimilation scheme "FlowFit" with continuity and Navier-Stokes-constraints to interpolate the scattered velocity and acceleration data via continuous 3D B-Splines on a cubic grid to recover the smallest flow scales.

The measurements were enabled by a dedicated bubble fluid solution, which we developed for generation of long-lived helium filled soap bubbles, allowing for long-term optical flow measurements at large scales in gaseous media. We show visualizations of the large-scale circulation (LSC) using iso-surfaces the Q-criterion, that allow a glance into the turbulent structure of the flow and to spot some of the dynamic features of the LSC. By employing Proper Orthogonal Decomposition (POD) in the rotating frame of the LSC, we are able to model the oscillatory dynamics of the LSC using just the first three POD modes with a standard deviation from the full data set of less than 5 % utilizing only ~ 50% of the turbulent kinetic energy.

1. Introduction

Thermal convection, i.e. heat transport by moving fluid, is among the most important channels for heat transfer and ubiquitous in nature and technology. It affects our everyday life on a variety of scales ranging from stellar to microscopic dimensions. Rayleigh-Bénard convection (RBC), where a fluid is heated from below and cooled from above in a well-defined way, is the most generic type of thermal convection and a configuration ideally suited to study the fundamentals of buoyancy driven flows (Bodenschatz et al., 2000; Chillà & Schumacher, 2012). Usually, RBC is characterized by three dimensionless parameters, which are the aspect ratio Γ of the sample, defined by the ratio

of sample diameter D and L height ($\Gamma = D/L$), the Rayleigh number Ra and the Prandtl number Pr. While the Prandtl number is just the ratio of kinematic viscosity ν and thermal diffusivity κ, i.e. $Pr = \nu/\kappa$, the Rayleigh number Ra characterizes the actual thermal driving of the fluid by the applied temperature difference ΔT. It is a dimensionless measure of the ratio of buoyancy to dissipative forces and given by $Ra = \beta g L^3 \Delta T/(\nu\kappa)$. Herewith β and g denote the isobaric thermal expansion coefficient and the acceleration of gravity, respectively.

In many fluids of practical relevance, even for moderate temperature gradients, Ra is typically above a critical value such that the convective flow between the plates is rendered turbulent. A prominent feature of the turbulent RB system is the presence of a large-scale circulation (LSC), which develops from self-organization of the thermal plumes erupting from the top and bottom thermal boundary layers. In cylindrical samples with a high degree of symmetry, the complex short- and long-term dynamics of the LSC have been the subject of many studies in the past. Besides rotations, complete cessations and restarts (Brown & Ahlers, 2006b), Torsional oscillations (Funfschilling et al., 2008) and sloshing modes were observed (Xi et al., 2009). The long-term dynamics was even found to be influenced by the earths Coriolis force (Brown & Ahlers, 2006a). In cylindrical samples with aspect ratios ranging from 1/3 to 1, besides a single LSC state also vertically stacked, counter-rotating rolls were found (Weiss & Ahlers, 2011; Xi & Xia, 2008). Most of the above mentioned studies were performed using wall-mounted temperature probes, though some planar PIV measurements revealing the LSC have been reported already (Kunnen, RPJ (Rudie), 2008; Sun et al., 2005; Xi & Xia, 2008).

Although the complex dynamics of the LSC in turbulent RBC has gained much attention, direct volumetric measurements of the LSC are still rare. While tomographic PIV (Schiepel et al., 2018) or Lagrangian Particle Tracking (Bosbach et al., 2021; Liot et al., 2017; Paolillo et al., 2021; Schiepel et al., 2018) have been employed in the past, measurements at full spatial and temporal resolution covering the whole sample were still lacking until recently. The same holds for direct measurements of the complex dynamics of the velocity fields of the LSC.

The above mentioned studies were conducted using water as working fluid, which allows to choose from a variety of almost neutrally buoyant tracer particles with high light scattering efficiency (Raffel et al., 2018). However, measurements in gaseous flows on large scales, as required for turbulent RBC, require special tracer particles. For this purpose, sub millimeter helium filled soap bubbles have been established as the tracer of choice for mixed convective flows (Bosbach et al., 2009; Kühn et al., 2009, 2012) and recently for low speed wind tunnel (Gibeau et al., 2020; Novara et al., 2021; Scarano et al., 2015) and even free field tests (Spoelstra et al., 2019).

However, their application to RBC was impeded by the limited lifetime of the order of 10^2 s (Huhn et al., 2017).

To bridge some of the gaps deliberated before, we performed the experiments and analyses described in the following. We specifically report on spatially and temporally resolved measurements of turbulent RBC in a sample of aspect ratio one, employing Lagrangian Particle Tracking (LPT) of long-lasting, helium-filled soap bubbles, using the "Shake-The-Box" (STB) method (Schanz et al., 2016). The tracer particles, measuring only a few hundred microns, were illuminated by a high-power pulsed LED array and imaged by a multi-camera setup involving six scientific CMOS cameras. The STB measurement system was adapted and optimized to capture the flow in the complete sample allowing resolving the large- and small-scale turbulent structures. Measurement runs extending about ~ 1,100 free fall times were enabled by the novel bubble fluid solution.

2. Experimental Set-Up

A dedicated convection experiment was developed for this study (Bosbach et al., 2021), which allows generating classical turbulent RBC and at the same time application of time-resolved LPT in the complete sample volume (Fig. 1). For details regarding the RBC apparatus and the experimental set-up, which is shortly outlined in the following, the reader is referred to (Bosbach et al., 2021).

The convection cell has an aspect ratio Γ of one and a height of 1.1 m. By using air at atmospheric pressure as working fluid, we reached Rayleigh numbers up to $Ra = 1.5 \cdot 10^9$ at $Pr = 0.70$. Due to the large dimensions of the experiment, tracer particles with high scattering efficiency were required. Hereto, we used helium filled soap bubbles (HFSB) with a mean diameter of 370 μm, generated by the orifice nozzle type of DLR (Bosbach et al., 2009). As we were interested in the long-term dynamics of the flow, a special bubble film solution (BFS) with extended HFSB life-time was required, which we developed specially for this purpose. Our in-house BFS allows for a mean bubble residence time of ~ 330 s (Bosbach et al., 2021), which is significantly enhanced as compared to the lifetimes achieved with commercial fluids, which are of the order of ~ 100 s (Huhn et al., 2017).

To ensure illumination of the tracer particles in the complete sample volume, we installed an array of 849 pulsed high-power LEDs about 1 m above the cooling plate. Particle images were captured by an inline ensemble of six scientific CMOS cameras with a resolution of 2560 x 2159 pixels each.

They were mounted on a circle around the convection cell at a distance of 3 m from the vertical center line and covered an aperture of 69°.

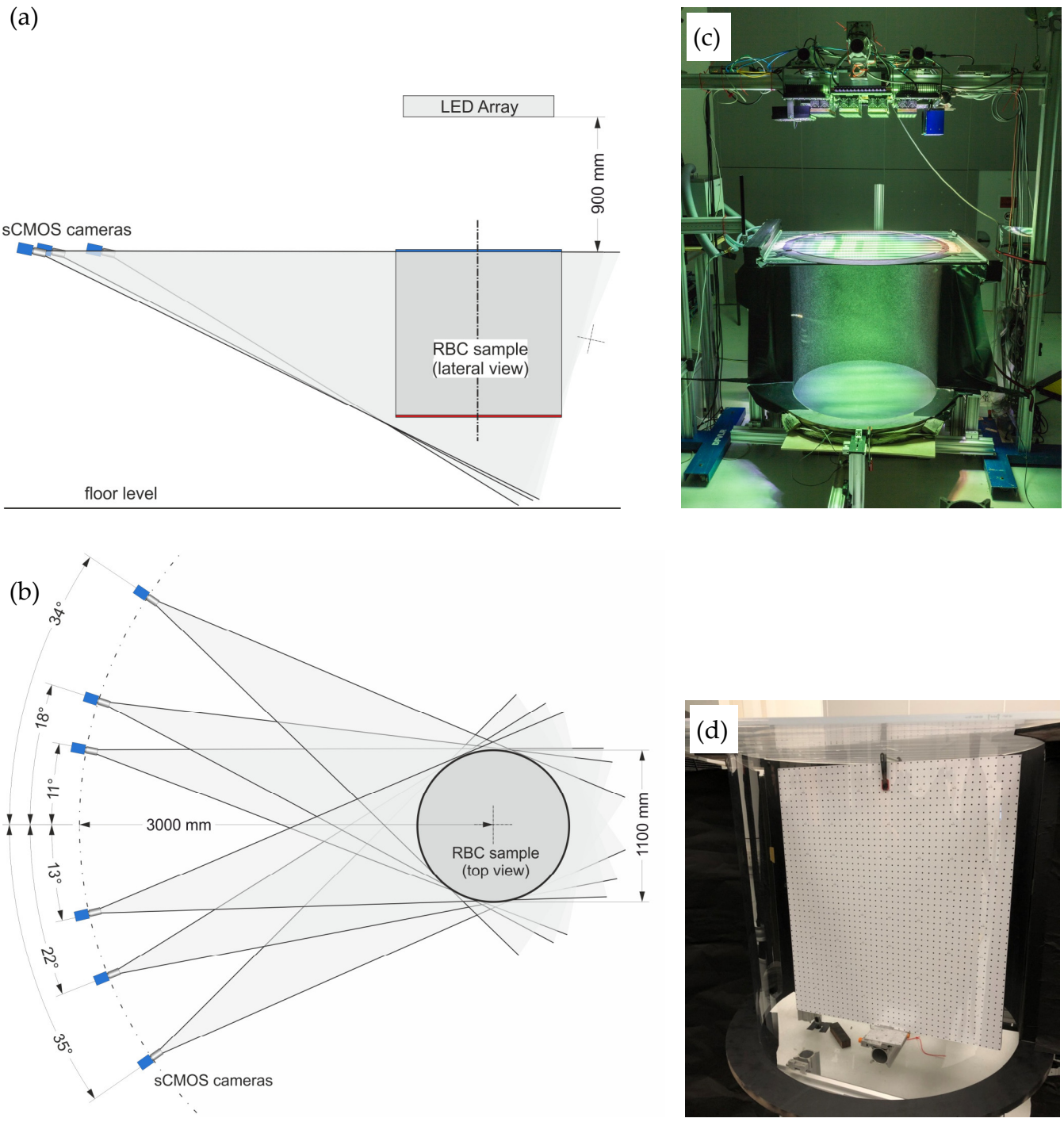

Fig. 1: (a, b) Optical set-up and (c) convection cell for time-resolved LPT with orifice nozzle of DLR generating long-lived HFSB. (d) Target inside the sample volume during calibration of the camera system.

To prevent blooming of the images due to the illuminated cooling plate, the cameras were adjusted with a sweeping view over the cooling plate and with an oblique view on the heating plate. The latter was covered with black acrylic foil to minimize surface reflections.

We calibrated the camera system using a calibration plate with a dot-pattern (spacing 25 mm), which we placed in three parallel planes with a consecutive distance of 230 mm within the cell (Fig. 1). The geometrical calibration was refined using Volume Self Calibration (VSC, Wieneke 2008) and calibration of the optical transfer function (OTF, Schanz et al. 2013). An iterative application of VSC allows to minimize global and local calibration errors to low subpixel values, as long as the optical distortions can be captured by the applied numerical camera model (in our case second order distortions can be accounted for). However, due to the presence of interfaces (e.g. windows), localized distortions may be introduced that the camera model cannot account for. In this case the cameras view through a curved plexiglass wall, leading to non-negligible shifts of the particle image projection point - especially close to the outer borders, where the viewing angles become more and more extreme. To account for such localized distortions, a 2D-shift map is calibrated by averaging the disparities between the projection points of the tracked 3D particles and the detected peak positions for each camera (Schanz et al. 2019). Fig. 2 shows the result of the shift-calibration for a selected camera. Upon querying the calibration, the found local shift is simply added to the projection point. The use of this further calibration enhancement allows for a significantly improved tracking fidelity close to the cell wall.

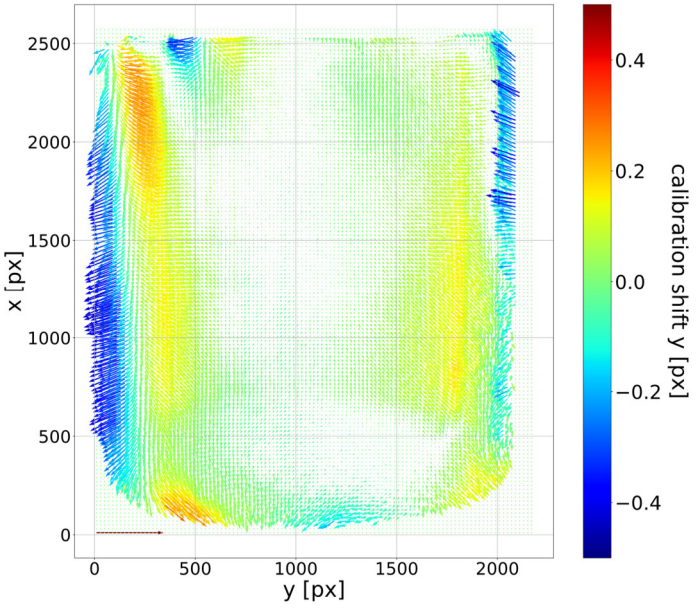

Fig. 2: Calibrated shift-map of single camera to account for optical distortions introduced by viewing through the curved plexi-glass wall. Decalibrations of up to 0.7 px were registered (the arrow in the lower left corner represents 1 px shift).

3. Experimental Conditions and Measurement Procedure

We studied RBC at different *Ra* numbers in the classical turbulent regime. Tab. 1 and 2 summarize the boundary conditions and fundamental parameters of the data-set discussed in the following. As a measure for the smallest / fastest scales in the flow to occur we determined the Kolmogorov length and time-scales, η_K and τ_η, which we deduced from the volume-averaged energy dissipation rate using a relation derived by Sugiyama et al. (2007)

$$\varepsilon_u = \nu^3 L^{-4} Pr^{-2} Ra(Nu - 1) \quad (1)$$

Herewith, Nu denotes the Nusselt number $Nu = QL/(\lambda \Delta T)$ with Q being the convective heat flux and λ the thermal conductivity. The second relevant length scale in our flow is the thickness of the thermal boundary layers, from which the thermal plumes are emitted. It is usually estimated from Nu as (Chillà & Schumacher, 2012)

$$\lambda_b = 1/(2Nu) \quad (2)$$

To determine Nu, which is required to evaluate (1) and (2), we used the data of Threlfall (1975). Finally, as an upper limit of the velocities to occur in the flow, the "free-fall" velocity U_f is given as evaluated by (Chillà & Schumacher, 2012)

$$U_f = \sqrt{\beta g \Delta T L} \quad (3)$$

Tab. 1: Boundary conditions and fundamental parameters of the presented flow case. For ΔT, ⟨T⟩ and *Ra*, the maximal deviations occurring during the STB measurement are denoted.

run #	ΔT [K]	⟨T⟩ [°C]	*Ra* [10^8]	*Pr*	η_K [mm]	τ_η [s]	λ_b [mm]	U_f [m/s]
30	11.8 ± 0.2	22.14 ± 0.17	15.3 ± 0.3	0.70	1.7	0.18	8.5	0.66

Tab. 2: Experimental settings and measurement parameters for the presented flow case. Herewith, f_{acq}, D and N denote the acquisition frequency, the duty cycle of the LEDs and number of instantaneous recordings, respectively. N_f denotes the acquisition time in number of free fall times. Finally, the maximal number of initially tracked particles n, the mean interparticle distance Δ/η_K, and the temporal oversampling $\tau_\eta \cdot f$ are specified.

run #	f_{acq} [Hz]	D [%]	N	N_f	n [1/cm³]	Δ / η_K	$\tau_\eta \cdot f$
30	30	9	54528	1091	0.56	7.8	5.4

Prior to the measurement, the convection sample was given three to four hours of thermal equilibration. The temperature levels of heating (T_h) and cooling plate (T_c) were chosen such, that the mean sample temperature $\langle T \rangle = (T_h + T_c)/2$ equaled the mean room temperature in the surrounding

of the RBC apparatus in order to minimize any net parasitic heat fluxes through the side wall. Prior to the LPT measurements, the fluid was seeded with HFSB by temporally inserting the HFSB nozzle through a small opening in the side wall. In order to prevent induction of artificial flow structures, the nozzle direction was changed every 10 s. After seeding the flow, the system was given between three and four minutes to allow for the turbulence induced in excess to decay.

The acquisition rates were set depending on Ra, for 'run 30' we used 30 Hz allowing for direct recording of the images to the computer drive and hence to record long runs. Accordingly, the temporal oversampling amounted to 5.4 times with respect to the Kolmogorov frequency $1/\tau_\eta$. The illumination time of the LED arrays was set to 3 ms, corresponding to a duty cycle of 9%. As the lifetime of the tracer particles was limited, the seeding density decayed during the experimental runs. However, the initial seeding density amounted to more than 0.56/cm³ as deduced from the initially tracked number of particles, translating into mean inter-particle distance of ~ 8 volume-averaged Kolmogorov lengths.

4. Data Processing

The raw particle image data was processed using the DLR in-house implementation of the "Shake-The-Box" LPT algorithm (Schanz et al., 2016) after slight image pre-processing, which comprised subtraction of the sliding minimum of 36 consecutive images (weighted with a factor of 1.05) plus a constant of 40 counts. A section of 200 x 200 pixels from the central part of one of the cameras is shown in Fig. 3 to illustrate the various stages of the image processing. As can be seen by comparison of the raw image with the minimum image, the former still suffers from a high level of background, which the minimum image discloses to consist of noise as well as pixels of different sensitivity in addition to HFSB sticking at the viewport and the background of the sample. Especially the latter are quite abundant due to the fact, that the data shown was taken more than 25 minutes after injecting the tracer particles. However, they could be removed efficiently by the procedure described above, revealing the actual particle images with good contrast and dimensions of 2-3 pixels. Due to the finite size-distribution of the HFSB and the spatially varying intensity of the LED illumination, the brightness of the particle images varies, requiring a proper fine-adjustment of the evaluation parameters, pondering the ability to track as many particles as possible while still keeping noisy tracks and ghost particles at a minimum.

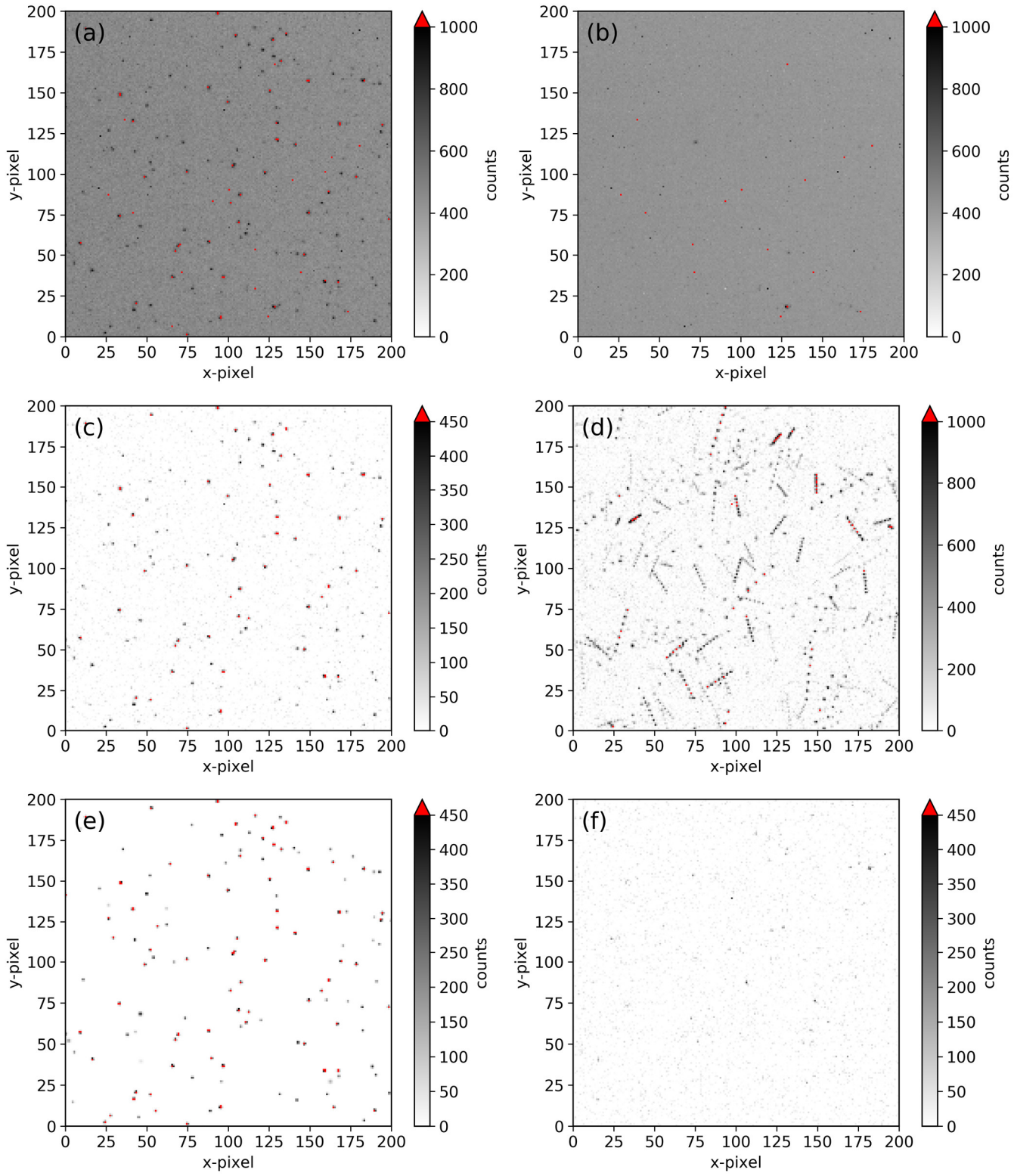

Fig. 3 Particle images in detail view. (a) Raw image, (b) minimum image, (c) pre-processed image, (d) pre-processed images accumulated over seven consecutive time-steps, (e) image of tracked and reprojected particles, (f) residual image, i.e. the difference between (c) and (e). Data from run 30 at timestep 40,010 (1334 s).

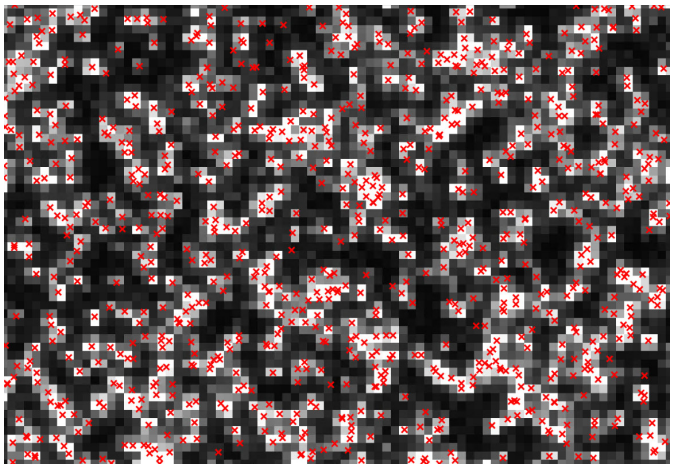

Fig. 4 Excerpt of camera image at central position (grayscale), with overlaid projection points of tracked particles (red crosses) at locally 0.18 *ppp*.

The accumulated particle image reveals, that the particles in the given field of view have a vastly varying velocities, caused by the turbulent nature of the flow and the large depth of field of the optical system (Fig. 3 (d)).

The STB method employs a predictor/corrector approach, in which known tracks are first extended to the next time-step and subsequently treated by a position correction method ('shaking' with image matching techniques). This way, the majority of particles can be tracked effortlessly and avoiding ghost particle generation, before the small portion of yet untracked particles is identified using (advanced) Iterative Particle Reconstruction IPR (Jahn et al., 2021; Wieneke, 2013). Herewith, images with locally up to 0.18 particles per pixel (ppp) could be evaluated. As an example, even if for a much lower particle per pixel density, Fig. 3 (e) depicts the reprojection of the tracked particles, which can be compared to the raw particle and pre-processed particle images in Fig. 3 (a) and (c). The residual image, which remains after removal of all tracked and reprojected particles is given in Fig. 3 (f), disclosing that the vast majority of the particle images have been tracked with the given settings.

However, due to the limited residence time of the HFSB, during the extensive time-scale of the experiment, the number of tracks depends on the actual time-step. While at the beginning of the measurement, more than half a million of HFSB are tracked, just a few thousand HFSB are remaining in the end (after 30 minutes). With the second STB pass, running backward in time and using the particle positions and track information from the first pass, the number of tracked particles can be increased by about 10%. As an example of a more densely seeded image, Fig. 4 depicts the central region of a camera image with locally 0.18 ppp from the beginning of the series. Overlaid to the grayscale image of the particles are the back-projected positions of the tracked

particles. The figure illustrates the ability of the method described above to reconstruct particles in 3D from image regions, where individual particles are hard or even impossible do distinguish by simple visual inspection.

After the second pass of STB, the particle tracks were fitted with a cubic B-spline curve using the TrackFit algorithm (Gesemann et al., 2016), which acts as an 18dB per octave temporal low-pass filter on the particle tracks. Herewith, the optimal cut-off frequency was determined from the position spectrum of the raw particles to amount to 0.22 of the Nyquist frequency, meaning that approximately the lowest 22% of the frequencies of our signal are able to pass while the noise is blocked in the higher frequency range. The raw positional errors of the reconstructed particles, deduced from the high-frequency part of the position spectrum of the unfiltered tracks, amount to 50 μm in x- and y-as well as 100 μm in z-direction. The filtering process roughly halves these values. Herewith, the error of the resulting processed signal is dominated by the noise floor remaining in the low frequency part of the spectrum. From the fitted tracks, the velocity and acceleration values were calculated as derivatives of the B-spline curve. As a result, a velocity uncertainty of 0.34 mm/s in x- and y-direction as well as 0.68 mm/s in z-direction could be estimated. The latter corresponds, to a dynamic velocity range of up to ~ 900:1 in x- and y- as well as ~ 450:1 in z-direction.

As the final step, the data assimilation scheme FlowFit (Gesemann et al., 2016) with continuity and Navier-Stokes-constraints was used to interpolate the scattered velocity and acceleration data by continuous 3D B-Splines to a cubic grid, while increasing the spatial resolution beyond the sampling by the particles due to the physical regularization. The results give access to the full velocity gradient tensor, thereby allowing for e.g. usage of derivative based visualization measures such as the Q-criterion.

5. Results

5.1 Visualizations of the Large-Scale Circulation

With the procedure elaborated above, we were able to resolve the turbulent large- and small-scale structures of the flow in our apparatus covering the complete sample volume. Especially after data-assimilation, the flow features can be extracted and visualized in a variety of ways. As an example, Fig. 5 shows iso-surfaces of the Q-criterion (Haller, 2005), color coded with the vertical velocity together with a horizontal slice of the vertical velocity at mid-height of the RBC-cell.

Herewith, instantaneous flow fields are visualized in a series of six with a period of 250 time-steps (8.33s). Using the iso-surfaces of Q for visualization allows us to gain insight into the complete sample volume, as small-scale turbulence is faded out. For data assimilation of the scattered particle data, we used a grid spacing of 7 mm (~ $4 \cdot \eta_K$) to regularize the data, corresponding to 0.13 ppc inside the sample. With the resulting B-spline coefficients, we sampled the data in Fig. 5 to an even finer grid with a step-size of 3.5 mm (~ $2 \cdot \eta_K$) in each direction.

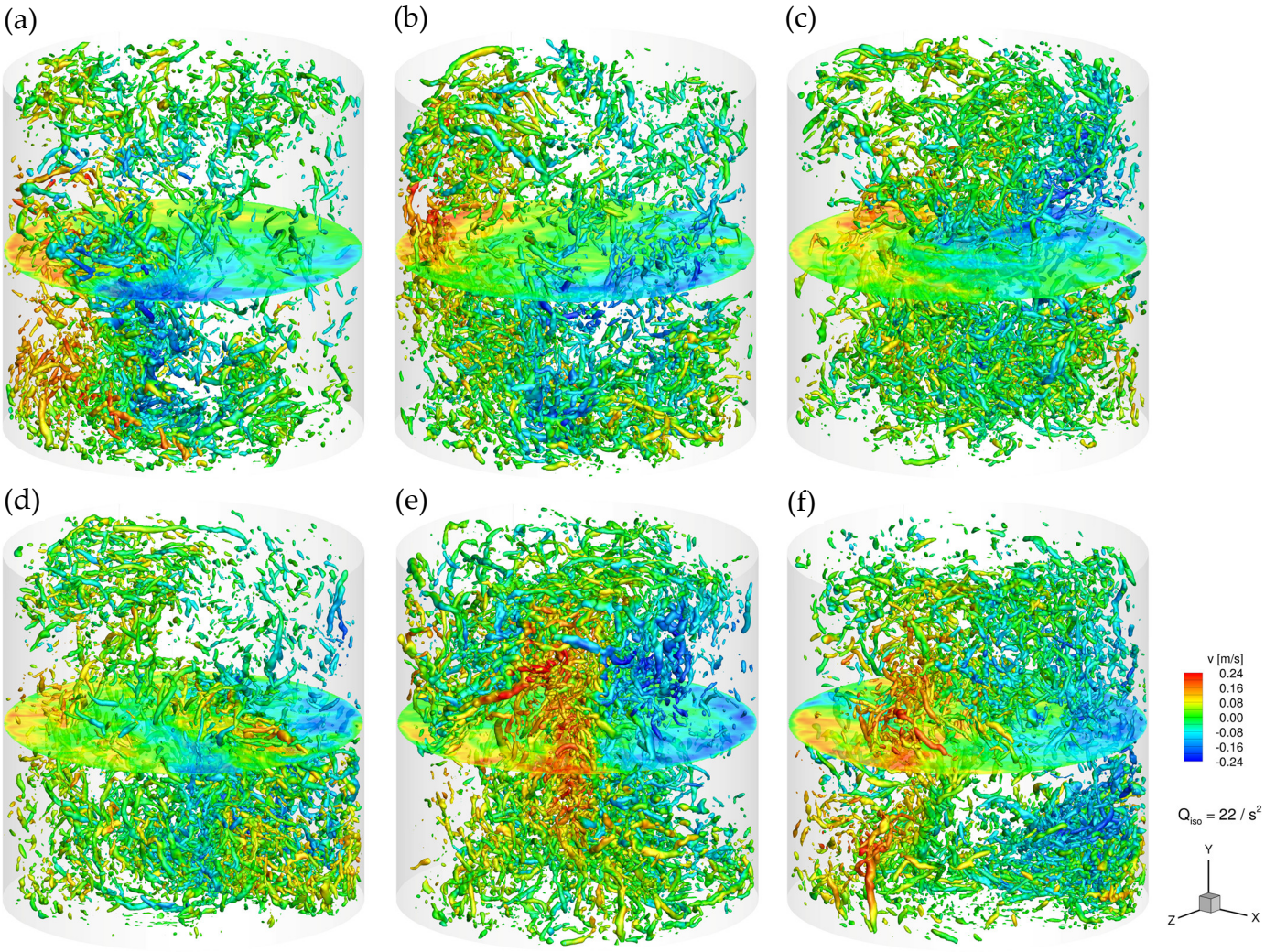

Fig. 5 Visualization of instantaneous turbulent velocity fields from RBC at $Ra = 1.5 \cdot 10^9$ measured with STB. Iso-surfaces of the Q-criterion visualized after data-assimilation using FlowFit, color-coded with the vertical velocity component (color). Time-span between snapshots (a) to (f): 250 time-steps (8.33 s).

In the visualizations, the footprints of the LSC can be spotted clearly by upwelling fluid on the left-hand side and downwelling fluid on the opposite side of the given views. Further, a variety of intermediate and small-scale structures with aspect ratios spanning more than one order of magnitude can be observed, illustrating the turbulent nature of the flow at the current *Ra*. Anyway,

despite the complexity of the flow, caused by the high turbulence level, the sloshing motion of the LSC can be observed clearly in the given snapshots, letting the LSC move from the front of the sample (in the given view) to the middle, the back and so forth. At the same time, the azimuth of the LSC fluctuates between the snapshots. Though the flow unveils a high level of non-stationarity and so does the LSC, some key features can be already spotted in this limited number of views: First, elongated vortical structures are evolving where the flow detaches from the heating / cooling plates after surpassing these. Secondly, corner rollers can be spotted where the LSC flow detaches from the lateral walls in the following after rising / falling along the side-walls.

5.2 Dynamics of the Large-Scale Circulation

In order to elaborate on the above described features of the flow and to obtain a view on the short-term dynamics and long-term behavior of the LSC, we calculated spatial statistics from the particle data and plotted them as time-series in Fig. 6 and Fig. 7.

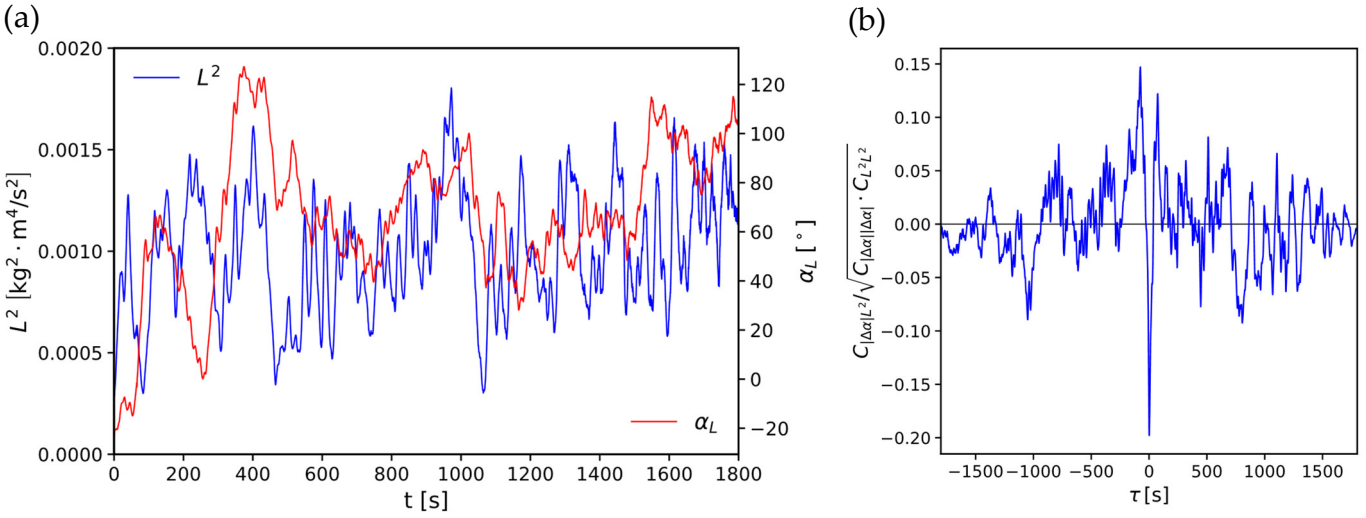

Fig. 6 Spatial statistic data as a function of time: (a) square of the total angular momentum (blue) and azimuth of the angular momentum (red), (b) correlation between square of angular momentum and azimuthal changes.

As measures for the strength ('rotional energy') and orientation of the LSC, the magnitude square (L^2) and azimuth (α_L) of the total angular momentum of the fluid, determined from the positional and velocity information of the tracked particles, are given in Fig. 6 (a). Herewith, the angular momentum was calculated with respect to the sample center. Besides slow meandering of the azimuth α_L ('rotation'), several events involving large angular reorientations, sometimes in combination with a breakdown of rotational energy can be spotted. Correlation of the square of the angular momentum and the azimuthal changes $|\Delta\alpha|$ between each timestep (Fig. 6 (b))

discloses, in fact, a noticeable anticorrelated contribution of -0.2 at $\tau = 0$, however, non-vanishing correlation signals for $|\tau| > 0$ indicate that possibly further reorientation mechanisms are present in the data as well.

For analysis of the fine-dynamics of the LSC, we calculated the angular momentum individually for the upper and lower third of the sample and determined the difference in azimuth between both, $\Delta\alpha^{TB}$. The result is plotted in Fig. 7 (a). Therein, the torsional oscillations of the LSC, known from indirect measurements of local wall temperatures (Funfschilling et al., 2008; Zhou et al., 2009), are disclosed by a very periodic oscillation of $\Delta\alpha^{TB}$, the amplitude reaching values of up to 80°. To further check whether the sloshing mode (Zhou et al., 2009) is present in our data as well, we calculated the center of gravity of the projection of the angular momentum to the LSC axis, ΔX_α^{COG} (normalized to L/2). Its plot versus time discloses that, in fact, a sloshing motion of the LSC occurs at the same frequency as the twisting mode. The time constant of these processes, which has been used to normalize the x-axis in Fig. 7, could be determined to amount to $\tau_{SL} = 28.5$ s by looking at the autocorrelations of each, ΔX_α^{COG} and $\Delta\alpha^{TB}$ and measuring the position of the first side maximum, see dotted lines in Fig. 7 (b).

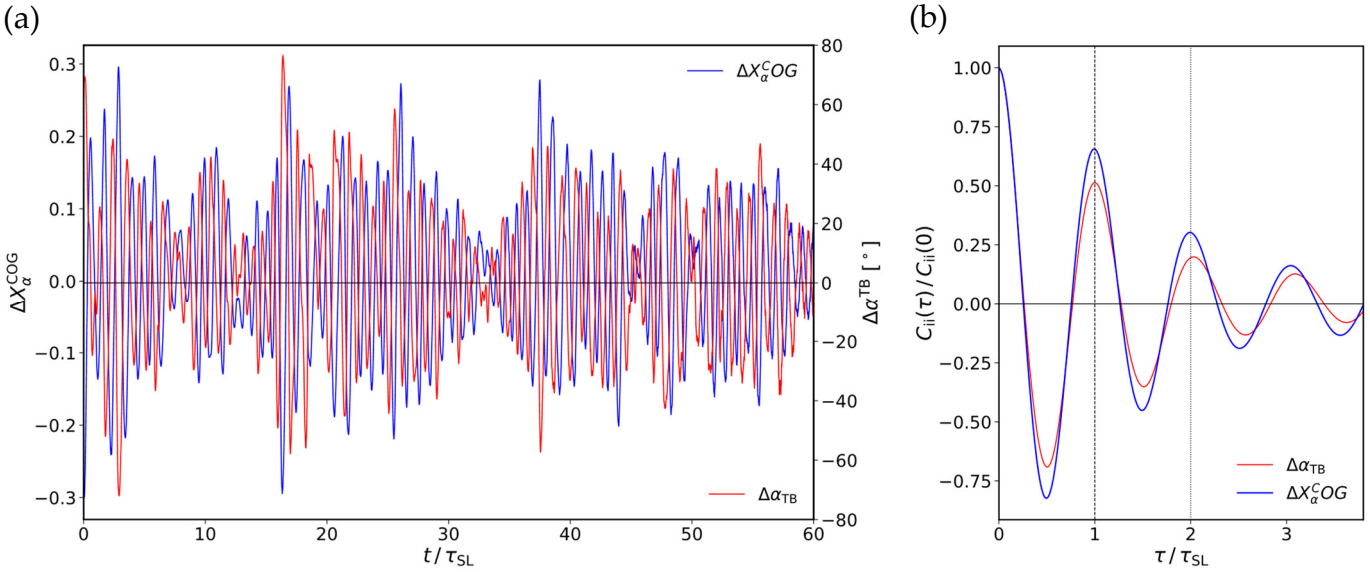

Fig. 7 Torsional oscillation and sloshing mode of the LSC: difference of azimuth of the total angular momentum in the upper and the lower third of the sample, $\Delta\alpha^{TB}$, and center of gravity of the projection of the angular momentum on the LSC axis, ΔX_α^{COG}.

5.3 Proper Orthogonal Decomposition of the Large-Scale Circulation

With the aim to decompose the dynamics of the LSC into individual modes or combinations of single modes and hence prepare the way for a reduced order model of the LSC dynamics, we performed Proper Orthogonal Decomposition (POD, see e.g. (Berkooz et al., 1993)) of the

instantaneous velocity data in the frame of the rotating LSC. We used the LSC azimuth of the total angular momentum α_L (see Fig. 6) to transform the particle velocity data into the rotating coordinate system. In this frame of reference, the LSC is oriented in the x,y-plane. To this data we applied FlowFit to assimilate the data on a grid with a spacing of 20 mm. We employed this comparably coarse grid here, as the seeding density decayed during the experiment and we wanted to have a significant number of particles per cell remaining at the end of the time series under investigation, which extended until $t / \tau_{SL} \cong 41$, taking into account every 20^{th} time step. As a result, the number of particles per cell (of the regular grid) varied between 3.9 ppc at the beginning and 0.11 ppc in the end. In fact, further extension of the time series would be possible using a multi-grid approach as well in a more sophisticated attempt. However, the chosen grid spacing, corresponding to $12 \cdot \eta_K$, that we further refined using the B-Spline coefficients to a step size of 10 mm, gives us rise to the assumption that the respective data covers all coherent turbulent structures relevant to the following analysis.

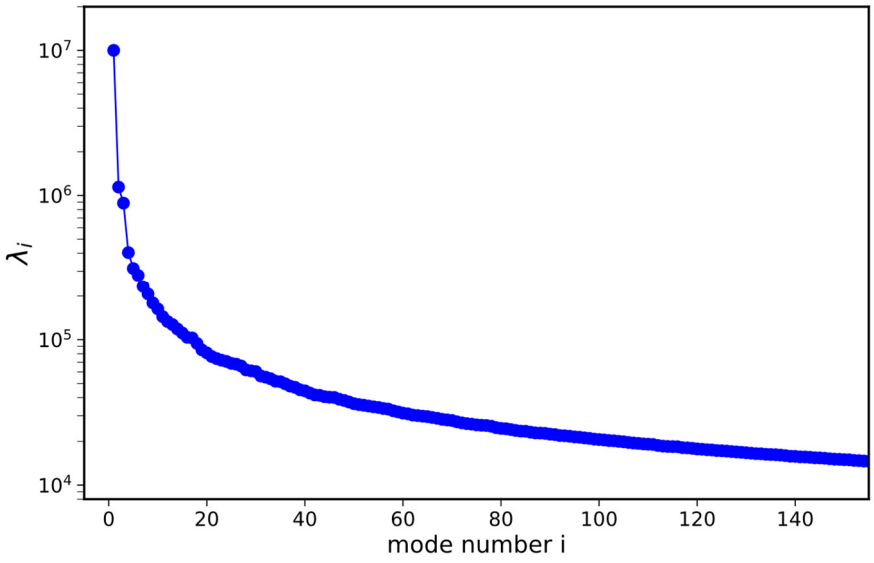

Fig. 8 Spectrum of the POD energy eigenvalues

A view to the spectrum of the energy eigenvalues (Fig. 8) discloses a qualitatively different progression for the first three and the other modes. Hereinafter, the first three modes, which carry most part of the dynamic information of the LSC, are given attention to as the further modes to a certain extent contain predominantly information required to describe the turbulence cascade. Fig. 9, Fig. 10 and Fig. 11 depict the first three POD modes as iso-surfaces of the three velocity components. Further, the corresponding time-coefficients are plotted in Fig. 12.

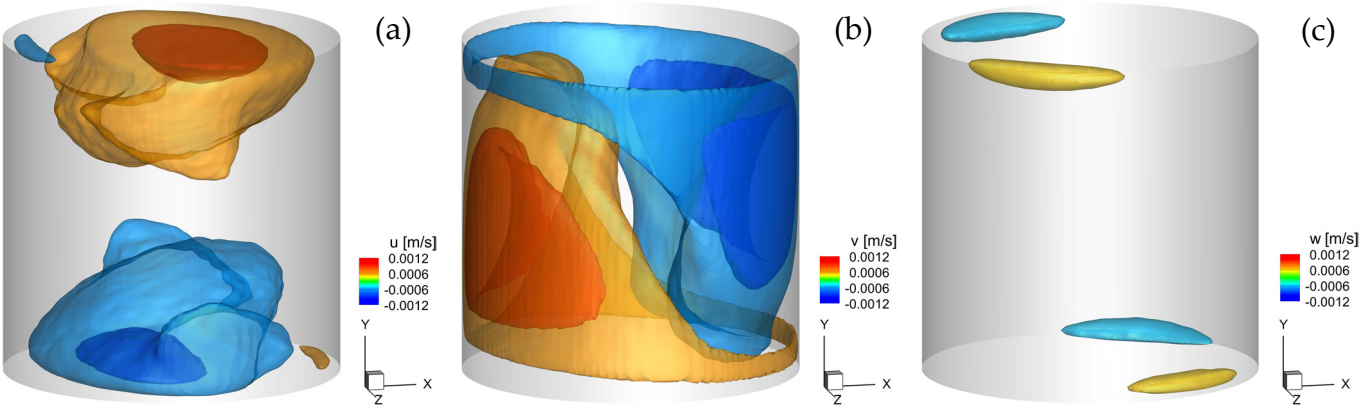

Fig. 9 First POD mode of the turbulent RBC in the rotating frame of the LSC. For details see text.

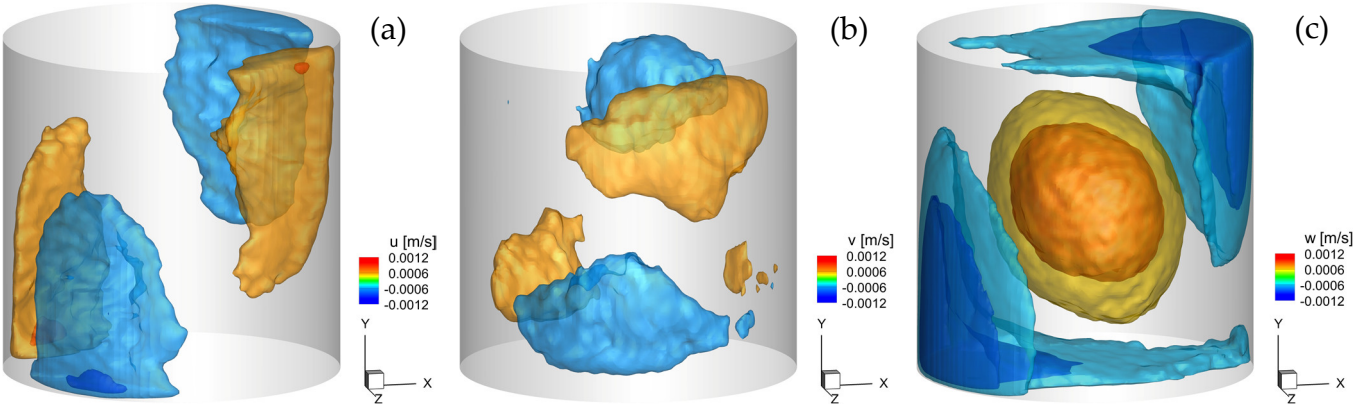

Fig. 10 Second POD mode of the turbulent RBC in the rotating frame of the LSC. For details see text.

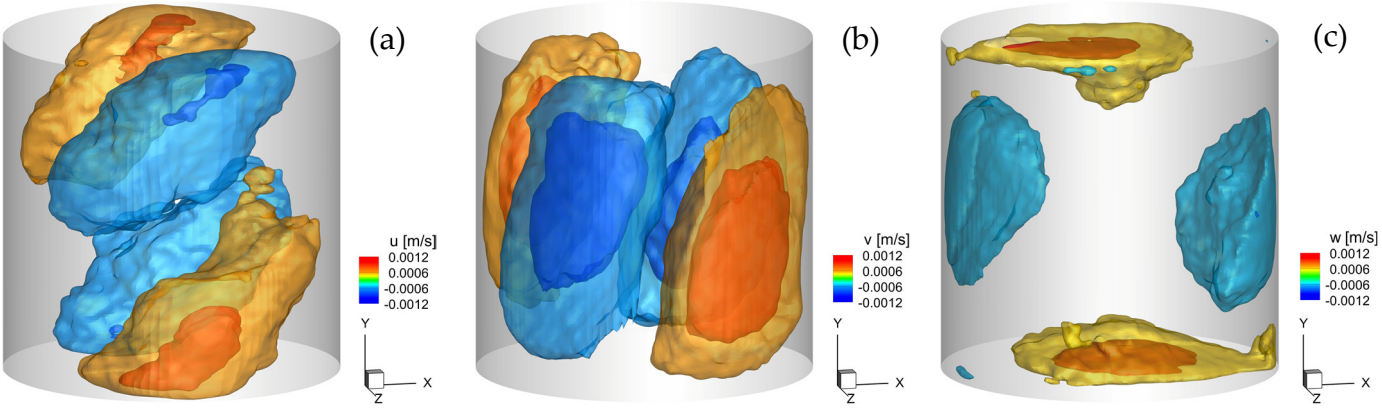

Fig. 11 Third POD mode of the turbulent RBC in the rotating frame of the LSC. For details see text.

We can, by looking at Fig. 12 (a), already state that the second and third mode, which oscillate very periodically, describe the short-term dynamics of the flow. The first mode, which shows a transient behavior, in turn represents the mean velocity field, which is corrected to cover the short-term dynamics with the coefficients of the other two modes. By looking at Fig. 9 (a) and (b), in fact, the

up- and down-welling of an LSC can be spotted in the iso-surfaces of u and v. Further, the characteristic corner-rollers of the up- and down-welling mean flow, occurring upon separation from the sidewall prior to attaching to the cooling and heating plate, can be spotted, respectively. The w-component, oriented perpendicular to the LSC in turn, carries only very small velocity contributions in the first mode. The second mode, in contrast, has its dominant contribution in exactly this component, see Fig. 10 (f), from which its impact on the LSC dynamics becomes clear: When combined with the first mode, it will turn the direction of the main flow over the heating and cooling plate. While the second mode has the same sign near both plates, the main flow is oriented in opposite directions (see mode 1), resulting in a twisting of the LSC flow there. The contributions of mode 2 to the other velocity components support this leverage on the LSC accordingly. We hence refer to the second POD mode as the "twisting" mode in the following. The third mode, finally, with its main contributions in the x and y direction, obviously tends to shift the LSC back and forth into the z-direction, i.e. perpendicular to the LSC, by proacting or counteracting the rotation of the LSC in the front or rear part (with respect to z) of the volume (Fig. 11). As a result, combination with the first mode leads to a sloshing of the LSC in z-direction and we hence refer to the third mode as the "sloshing" mode hereinafter.

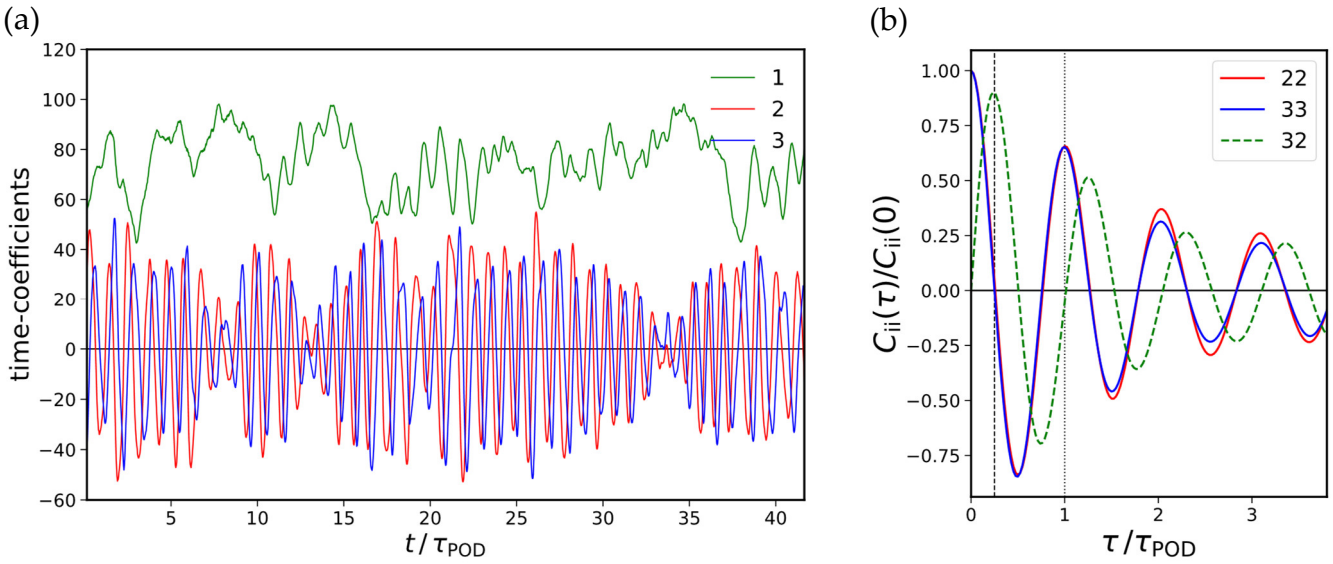

Fig. 12 (a) Time-coefficients of the first three modes and (b) auto-correlation of the second and third mode as well as cross-correlation between the third ("sloshing") and second ("twisting") POD mode. For details refer to the text.

In order to shed some light on the dynamics captured by these modes, the time-coefficients of the first three modes are depicted in Fig. 12 (a). While the time-coefficient of the first mode unveils a quasiperiodic behavior, congruent with the time-development of the angular momentum in Fig. 6, those of the second and third mode disclose a very periodic time-dependence, seemingly phase-

locked to each other. In order to verify this impression, we determined and plotted the auto- and cross-correlation functions of the second and third time-coefficient in Fig. 12 (b). The characteristic period of the second and third mode, determined from the position of the first side-maxima of the autocorrelation functions, turns out to be τ_{POD} = 28.0 s for both. This value is very similar to the sloshing period determined in section 5.2 to τ_{SL} = 28.5 s. Further, the cross-correlation of both time-coefficients discloses, in fact, phase-locking of the two modes with a relative phase of $\pi/2$ (dashed line in Fig. 12 (b)). The latter is in perfect agreement with the phase shift of $\pi/2$ deduced for the twisting and sloshing mode from wall-temperature measurements (Zhou et al., 2009).

While it seems, that the first three POD modes are able to already model a lot of the complex dynamics of the LSC, we would like to know to which extent the LSC dynamics can be described with these few modes. To answer this question, we calculated the relative content of kinetic energy, angular momentum |L| and twisting angle $\Delta\alpha_{TB}$ in the reconstructed flow fields as compared to the measured fields, respectively ($\Delta\alpha_{TB}$ was referred to 180°). While the mean of the relative kinetic energy amounts to about 54%, the rms values of the deviations of the other quantities amount ~4.1% for the relative angular momentum and 3.3% for the twisting angle. While these average values are a good estimate of the overall performance, we would like to note that in several, even if very time-limited phases of the series, deviations temporally larger than 10% percent occur, requiring much more POD modes to model the more complex behavior of the LSC. This holds especially when the LSC undergoes strong reorientations, accompanied by a breakdown of the rotational energy. It is expectable, that during such phases the motion comprises more complex motional patterns than just rotation, sloshing and twisting. However, analysis and modeling of the transitional phases is beyond the current article and will be addressed in further studies.

6. Conclusions

We have demonstrated that by combination of STB / LPT with long-lived HFSB, simultaneous acquisition of Lagrangian particle tracks and time-resolved Eulerian Velocity fields of turbulent RBC becomes possible in large samples of gaseous fluids. Specifically, we achieved scale-resolving measurements in the entire volume of a cylindrical RBC-sample of aspect ratio one with a characteristic length of L = 1.1 m.

The generated data sets allow for direct observation of the interaction of large- and small-scale turbulent structures, e.g. by filtering using the Q-criterion. Having conducted runs as long as 30

minutes, our data allows for direct studies of the short and long-term dynamics of the Large-Scale Circulation including torsional oscillations, sloshing, azimuthal meandering and spontaneous reorientations. By analyzing the particle tracks in the Eulerian frame, we could identify the oscillatory dynamics of the LSC comprising “sloshing” and “twisting” mode. Decoupling of these dynamic modes from the LSC becomes possible by POD analysis of the velocity data in the rotating frame of the LSC azimuth. Herewith, the first mode is found to represent the mean flow / LSC, while the second and third mode constitute the *torsional* oscillation and the *sloshing* of the LSC, respectively. As a result, with just three modes, covering slightly more than one half of the total kinetic energy of the flow in average, we can model the angular momentum and twisting angle with a standard deviation from the full data set of less than 5 %.

Acknowledgements

This work was supported by the Deutsche Forschungsgemeinschaft (DFG) through Grant No. SCHR 1165/5-1 as part of the Priority Programme on Turbulent Superstructures (DFG SPP 1881). Support with Hard- and Software by LaVision GmbH is gratefully acknowledged. We thank Jonathan Lemarechal, Tobias Kleindienst and Carsten Fuchs for their contributions to the RBC sample and Janos Agocs for his support during set-up of the optical system. We are grateful to the Max-Planck-Institute for Dynamics and Self-Organization in Göttingen for provision of the thermal bath for the experiments.

References

Berkooz, G., Holmes, P., & Lumley, J. L. (1993). The Proper Orthogonal Decomposition in the Analysis of Turbulent Flows. *Annual Review of Fluid Mechanics*, *25*(1), 539–575. https://doi.org/10.1146/annurev.fl.25.010193.002543

Bodenschatz, E., Pesch, W., & Ahlers, G. (2000). Recent developments in Rayleigh-Bénard convection. *Annual review of fluid mechanics*, *32*(1), 709–778.

Bosbach, J., Kühn, M., & Wagner, C. (2009). Large scale particle image velocimetry with helium filled soap bubbles. *Experiments in Fluids*, *46*(3), 539–547. https://doi.org/10.1007/s00348-008-0579-0

Bosbach, J., Schanz, D., Godbersen, P., & Schröder, A. (2021). Spatially and temporally resolved measurements of turbulent Rayleigh-Bénard convection by Lagrangian particle tracking of long-lived helium-filled soap bubbles. *14th International Symposium on Particle Image Velocimetry*, *1*(1). https://doi.org/10.18409/ispiv.v1i1.208

Brown, E., & Ahlers, G. (2006a). Effect of the Earth's Coriolis force on the large-scale circulation of turbulent Rayleigh-Bénard convection. *Physics of Fluids*, *18*(12), 125108. https://doi.org/10.1063/1.2402875

Brown, E., & Ahlers, G. (2006b). Rotations and cessations of the large-scale circulation in turbulent Rayleigh–Bénard convection. *Journal of Fluid Mechanics*, *568*, 351. https://doi.org/10.1017/S0022112006002540

Chillà, F., & Schumacher, J. (2012). New perspectives in turbulent Rayleigh-Bénard convection. *The European Physical Journal E*, *35*(7). https://doi.org/10.1140/epje/i2012-12058-1

Funfschilling, D., Brown, E., & Ahlers, G. (2008). Torsional oscillations of the large-scale circulation in turbulent Rayleigh–Bénard convection. *Journal of Fluid Mechanics*, *607*. https://doi.org/10.1017/S0022112008001882

Gesemann, S., Huhn, F., Schanz, D., & Schröder, A. (2016). From Noisy Particle Tracks to Velocity, Acceleration and Pressure Fields using B-splines and Penalties. *18th International Symposium on the Application of Laser and Imaging Techniques to Fluid Mechanics*, 17.

Gibeau, B., Gingras, D., & Ghaemi, S. (2020). Evaluation of a full-scale helium-filled soap bubble generator. *Experiments in Fluids*, *61*(2), 28. https://doi.org/10.1007/s00348-019-2853-8

Haller, G. (2005). An objective definition of a vortex. *Journal of Fluid Mechanics*, *525*, 1–26. https://doi.org/10.1017/S0022112004002526

Huhn, F., Schanz, D., Gesemann, S., Dierksheide, U., van de Meerendonk, R., & Schröder, A. (2017). Large-scale volumetric flow measurement in a pure thermal plume by dense tracking of helium-filled soap bubbles. *Experiments in Fluids*, *58*(9). https://doi.org/10.1007/s00348-017-2390-2

Jahn, T., Schanz, D., & Schröder, A. (2021). Advanced iterative particle reconstruction for Lagrangian particle tracking. *Experiments in Fluids*, *62*(8), 179. https://doi.org/10.1007/s00348-021-03276-7

Kühn, M., Bosbach, J., & Wagner, C. (2009). Experimental parametric study of forced and mixed convection in a passenger aircraft cabin mock-up. *Building and Environment*, *44*(5), 961–970. https://doi.org/10.1016/j.buildenv.2008.06.020

Kühn, M., Ehrenfried, K., Bosbach, J., & Wagner, C. (2012). Large-scale tomographic PIV in forced and mixed convection using a parallel SMART version. *Experiments in Fluids*, *53*(1), 91–103. https://doi.org/10.1007/s00348-012-1301-9

Kunnen, RPJ (Rudie). (2008). *Turbulent rotating convection*. Technische Universiteit Eindhoven. https://doi.org/10.6100/IR637592

Liot, O., Salort, J., Seychelles, F., Gasteuil, Y., Pinton, J.-F., & Chillà, F. (2017). Lagrangian Measurements in Turbulent Thermal Convection: About the Inhomogeneity of the Velocity and Temperature Fields. *Procedia IUTAM*, *20*, 112–119. https://doi.org/10.1016/j.piutam.2017.03.016

Novara, M., Schanz, D., Geisler, R., Agocs, J., Eich, F., Bross, M., Kähler, C., & Schröder, A. (2021). Investigation of turbulent boundary layer flows with adverse pressure gradient by means of 3D Lagrangian particle tracking with Shake-The-Box. *14th International Symposium on Particle Image Velocimetry*, *1*(1). https://doi.org/10.18409/ispiv.v1i1.70

Paolillo, G., Greco, C. S., Astarita, T., & Cardone, G. (2021). Experimental determination of the 3-D characteristic modes of turbulent Rayleigh–Bénard convection in a cylinder. *Journal of Fluid Mechanics*, *922*, A35. https://doi.org/10.1017/jfm.2021.554

Raffel, M., Willert, C. E., Scarano, F., Kähler, C., Wereley, S. T., & Kompenhans, J. (2018). *Particle Image Velocimetry: A Practical Guide* (3. Aufl.). Springer International Publishing. https://doi.org/10.1007/978-3-319-68852-7

Scarano, F., Ghaemi, S., Caridi, G. C. A., Bosbach, J., Dierksheide, U., & Sciacchitano, A. (2015). On the use of helium-filled soap bubbles for large-scale tomographic PIV in wind tunnel experiments. *Experiments in Fluids*, *56*(2), 42. https://doi.org/10.1007/s00348-015-1909-7

Schanz, D., Gesemann, S., & Schröder, A. (2016). Shake-The-Box: Lagrangian particle tracking at high particle image densities. *Experiments in Fluids*, *57*(5). https://doi.org/10.1007/s00348-016-2157-1

Schanz, D., Gesemann, S., Schröder, A., Wieneke, B., & Novara, M. (2013). Non-uniform optical transfer functions in particle imaging: Calibration and application to tomographic reconstruction. *Measurement Science and Technology*, *24*(2), 024009. https://doi.org/10.1088/0957-0233/24/2/024009

Schanz D, Schröder A, Novara M, Geisler R, Agocs J, Eich F, Bross M, Kähler CJ (2019) Large-scale volumetric characterization of a turbulent boundary layer flow. 13th Intern Symp on PIV 19 (No. 182, pp. 251-265). Uni BW München, D: AtheneForschung

Schiepel, D., Herzog, S., & Wagner, C. (2018). Experimental Study of Turbulent Rayleigh-Bénard Convection Using Large-Scale Tomo-PIV and High-Density PTV. In M. O. Deville, V. Couaillier, J.-L. Estivalezes, V. Gleize, T. HiêpLê, M. Terracol, & S. Vincent (Hrsg.), *Turbulence and Interactions* (Bd. 135, S. 225–231). Springer International Publishing. https://doi.org/10.1007/978-3-319-60387-2_24

Spoelstra, A., de Martino Norante, L., Terra, W., Sciacchitano, A., & Scarano, F. (2019). On-site cycling drag analysis with the Ring of Fire. *Experiments in Fluids*, *60*(6), 90. https://doi.org/10.1007/s00348-019-2737-y

Sun, C., Xia, K.-Q., & Tong, P. (2005). Three-dimensional flow structures and dynamics of turbulent thermal convection in a cylindrical cell. *Physical Review E*, *72*(2). https://doi.org/10.1103/PhysRevE.72.026302

Weiss, S., & Ahlers, G. (2011). Turbulent Rayleigh–Bénard convection in a cylindrical container with aspect ratio Γ = 0.50 and Prandtl number Pr = 4.38. *Journal of Fluid Mechanics*, *676*, 5–40. https://doi.org/10.1017/S0022112010005963

Wieneke, B. (2008). Volume self-calibration for 3D particle image velocimetry. *Experiments in Fluids*, *45*(4), 549–556. https://doi.org/10.1007/s00348-008-0521-5

Wieneke, B. (2013). Iterative reconstruction of volumetric particle distribution. *Measurement Science and Technology*, *24*(2), 024008. https://doi.org/10.1088/0957-0233/24/2/024008

Xi, H.-D., & Xia, K.-Q. (2008). Flow mode transitions in turbulent thermal convection. *Physics of Fluids*, *20*(5), 055104. https://doi.org/10.1063/1.2920444

Xi, H.-D., Zhou, S.-Q., Zhou, Q., Chan, T.-S., & Xia, K.-Q. (2009). Origin of the Temperature Oscillation in Turbulent Thermal Convection. *Physical Review Letters*, *102*(4). https://doi.org/10.1103/PhysRevLett.102.044503

Zhou, Q., Xi, H.-D., Zhou, S.-Q., Sun, C., & Xia, K.-Q. (2009). Oscillations of the large-scale circulation in turbulent Rayleigh–Bénard convection: The sloshing mode and its relationship with the torsional mode. *Journal of Fluid Mechanics*, *630*, 367–390. https://doi.org/10.1017/S0022112009006764